



Cite this: *Soft Matter*, 2017, **13**, 1463

# Phase diagram of elastic spheres

L. Athanasopoulou<sup>\*a</sup> and P. Ziherl<sup>ab</sup>

Received 2nd November 2016,  
Accepted 28th December 2016

DOI: 10.1039/c6sm02474b

[rsc.li/soft-matter-journal](http://rsc.li/soft-matter-journal)

Experiments show that polymeric nanoparticles often self-assemble into several non-close-packed lattices in addition to the face-centered cubic lattice. Here, we explore theoretically the possibility that the observed phase sequences may be associated with the softness of the particles, which are modeled as elastic spheres interacting upon contact. The spheres are described by two finite-deformation theories of elasticity, the modified Saint-Venant–Kirchhoff model and the neo-Hookean model. We determine the range of indentations where the repulsion between the spheres is pairwise additive and agrees with the Hertz theory. By computing the elastic energies of nine trial crystal lattices at densities far beyond the Hertzian range, we construct the phase diagram and find the face- and body-centered cubic lattices as well as the A15 lattice and the simple hexagonal lattice, with the last two being stable at large densities where the spheres are completely faceted. These results are qualitatively consistent with observations, suggesting that deformability may indeed be viewed as a generic property that determines the phase behavior in nanocolloidal suspensions.

## 1 Introduction

At large enough densities, polymeric nanocolloids such as dendrimers, star polymers, and block-copolymer micelles self-organize in a number of ordered structures. The phase sequence often includes the face- and body-centered cubic (FCC and BCC, respectively), A15, and  $\sigma$  lattices<sup>1–4</sup> as well as dodecagonal quasicrystals<sup>1,4–6</sup> and even the simple hexagonal (SH) lattice.<sup>4</sup> This behavior appears to be fairly non-specific, which suggests that it may be caused by particle softness as the common feature of the different macromolecular architectures. So far, this idea has been explored using simulations at a monomer-resolved level<sup>7,8</sup> or by relying on effective interactions.<sup>9</sup> A different type of argument may be sought within continuum theories, which dispose of most molecular-level details. The soap-froth model which postulates that the free energy of the particles includes bulk and surface terms<sup>10</sup> readily rationalizes the stability of the A15 lattice. Yet another perspective is to view the particles as elastic spheres which repel each other on contact. For small deformations, repulsion is pairwise additive and proportional to  $h^{5/2}$  according to the Hertz theory;<sup>11</sup> here  $h$  is the indentation of the contact zone. This power law gives rise to an elaborate phase diagram.<sup>12,13</sup>

The relevance of studies based on the Hertz theory is restricted to small indentations where the deformations of the neighboring

contact zones are independent. On compression, the spheres are transformed into truncated spheres, with the size of the contact zones increasing with indentation (Fig. 1). At some point, the neighboring contact zones begin to overlap and are thus no longer independent; this regime may be referred to as advanced faceting. In the FCC and BCC lattices, geometrical arguments suggest that the onset of advanced faceting, and thus the end of the Hertzian range, is at reduced indentations  $2h/\sigma \approx 0.13$  and  $0.22$ , respectively; here  $\sigma$  is the diameter of the reference undeformed sphere.<sup>†</sup> The physical criterion for the validity of the Hertz theory is more stringent: the theory is applicable if the displacement fields penetrating from the contact zones into the spheres do not interfere with each other.

Despite these limitations, it is instructive to sketch the phase diagram of Hertzian spheres at  $T = 0$ . For clarity, we only compare the FCC and BCC lattices previously identified as stable just beyond the fluid–solid transition.<sup>12,13</sup> The Hertzian energy of each contact zone is

$$F_H = \frac{8\sqrt{2}Y\sqrt{\sigma}}{15(1-\nu^2)}h^{5/2}, \quad (1)$$

where  $Y$  is the Young modulus and  $\nu$  is the Poisson ratio. At any density, the indentation of a given zone depends on the lattice type, with the lattices also differing in the number of neighbors pushing against the reference sphere. As shown in Fig. 1, the deformation energies of the two lattices are quite similar across a broad range of reduced number densities  $\rho\sigma^3$ , yet at  $\rho\sigma^3 \lesssim 2.154$

<sup>a</sup> Jožef Stefan Institute, Jamova 39, SI-1000 Ljubljana, Slovenia.  
E-mail: [labrinath@ijs.si](mailto:labrinath@ijs.si)

<sup>b</sup> Faculty of Mathematics and Physics, University of Ljubljana, Jadranska 19, SI-1000 Ljubljana, Slovenia

<sup>†</sup> Not to be confused with the name of the  $\sigma$  lattice,<sup>1</sup> a 30-site lattice of space group  $P4_2/mnm$ .

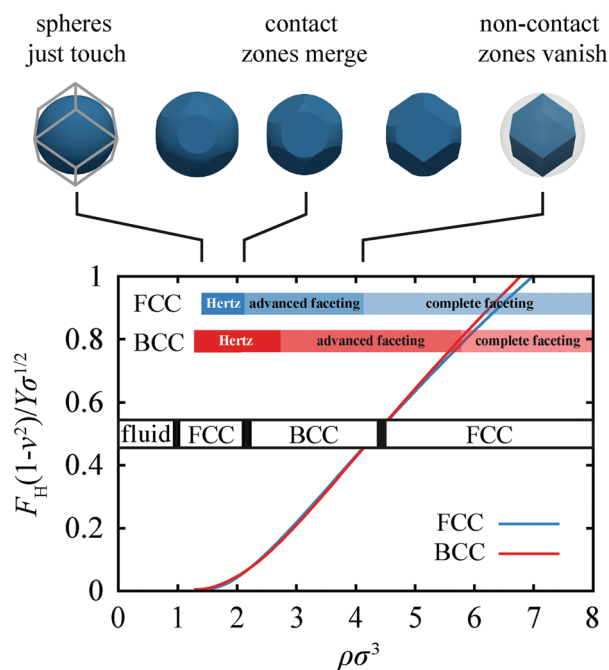


Fig. 1 Elastic energies of FCC and BCC lattices of Hertzian spheres vs. reduced density. The snapshots illustrate the Hertzian, advanced-faceting, and complete-faceting regimes of the FCC lattice defined using geometrical arguments; the frame and the transparent sphere illustrate the Wigner–Seitz cell at contact and the reference sphere at the onset of complete faceting, respectively. The blue and red banners show the corresponding density ranges for the FCC and BCC lattices, respectively. The phase sequence is indicated by the inset in the center, with the black stripes representing phase coexistence; the fluid–FCC transition at  $T = 0$  is reproduced from ref. 12.

the FCC lattice has a lower energy, whereas the BCC lattice is stable at  $\rho\sigma^3 > 2.301$ . Since the phase coexistence falls within the geometrical Hertzian ranges of both lattices, this theory of the transition appears to be self-consistent. But this is essentially all that one can expect from the Hertzian interaction because the two lattices enter the advanced-faceting regimes slightly beyond the transition. Any further conclusions are without proper grounds: for example, the BCC–FCC transition at  $\rho\sigma^3 \approx 4.5$  (also indicated in Fig. 1) involves the two lattices in the advanced and the complete faceting regimes and is thus meaningless. Like in ref. 12 and 13, additional trial lattices may be included in this analysis but none of them prevails in the Hertzian range.

Here, we study the zero-temperature phase diagram of identical elastic spheres, focusing on non-auxetic materials where the Poisson ratio is positive. Using two distinct finite-deformation models (Section 2), we compute the shape and the energy of spheres arranged in trial lattices in Table 1. In Section 3, we reanalyze the validity of the Hertz theory, finding that the fluid–FCC transition from ref. 12 is well within the Hertzian range but the solid–solid transitions<sup>12,13</sup> are not. We also quantify the onset of the regime where the stress distribution within the spheres is essentially uniform. Finally, we show that in the two models studied the phase sequence is either fluid–FCC–A15, fluid–FCC–BCC–A15, fluid–FCC–A15–SH, or fluid–FCC–BCC–A15–SH depending on the Poisson ratio and the model (Section 4).

## 2 The model

The deformation behavior of a material depends on the stress–strain relation determined by the strain energy density. Here, we study the modified Saint-Venant–Kirchhoff (SVK) model<sup>14</sup> and the neo-Hookean (NH) model.<sup>15</sup> In the former, the strain energy density is given by

$$f_{\text{SVK}}(\mathbf{F}) = \mu \text{tr}(\mathbf{E}^2) + \frac{1}{2} \lambda (\ln J)^2, \quad (2)$$

where  $\mathbf{E} = (\mathbf{F}^T \mathbf{F} - \mathbf{I})/2$  is the Green strain tensor,  $\mathbf{I}$  is the unit tensor, and  $\mathbf{F} = \mathbf{I} + \partial \mathbf{u} / \partial \mathbf{X}$  is the deformation gradient tensor (with  $\mathbf{u}$  and  $\mathbf{X}$  being the displacement and reference position of a point, respectively); the Jacobian  $J = \det \mathbf{F}$  gives the ratio of an infinitesimal volume element in the deformed body to its reference volume. In the SVK model, which is a direct generalization of the Hookean energy density, the volumetric term is proportional to  $(\ln J)^2$  and the moduli are the usual Lamé coefficients. In the NH model associated with polymer elasticity<sup>16–18</sup>




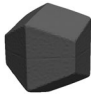
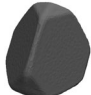
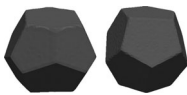



$$f_{\text{NH}}(\mathbf{F}) = \frac{1}{2} \mu (I_C - 3 - 2 \ln J) + \frac{1}{2} \lambda (J - 1)^2, \quad (3)$$

where  $I_C = \text{tr} \mathbf{C}$  and  $\mathbf{C} = \mathbf{F}^T \mathbf{F}$  is the right Cauchy–Green deformation tensor. This strain energy density differs from eqn (2) primarily in the volumetric term, which remains finite at  $J \rightarrow 0$ , and in the shear term which includes  $\ln J$  and thus diverges at  $J \rightarrow 0$ . In both models, the Lamé coefficients are expressed in terms of the Young modulus and Poisson ratio defined in the small-deformation regime:  $\mu = Y/[2(1 + \nu)]$  and  $\lambda = Y\nu/[(1 + \nu)(1 - 2\nu)]$ .

In this paper, the free energy of a given lattice is approximated by the elastic energy of the spheres, disregarding entropic effects. This is expected to provide an accurate description at large densities where the spheres are very deformed but not at the fluid–solid transition, which is covered by the Hertz theory.<sup>12</sup> The elastic energy of each lattice is computed within the cell model where the reference sphere is confined to a polyhedral Wigner–Seitz cell which mimics the cage formed by the neighboring spheres; the contact zones between the sphere and its neighbors lie at the faces of the cell. We compare the elastic energies of nine lattices chosen based on the existing insight<sup>12,13</sup> (Table 1). With the exception of the A15 lattice, all of them have a single type of lattice site and thus the implementation of the cell model is straightforward.

The A15 lattice contains two inequivalent sites which may be referred to as interstitial and columnar,<sup>10</sup> with their large-density coordination numbers being 12 and 14, respectively. This lattice is represented by two cells, and the force balance at the contact zones between the 12- and 14-coordinated sites is not ensured by symmetry like in single-site lattices. Here, the force balance is approximated by slightly adjusting the location of cell faces such that the volumes of the two inequivalent cell types are identical. Thus, at large compressions where the energy density within the deformed spheres is almost uniform and where the  $J$ -dependent energy terms are dominant, the pressures in the 12- and the 14-coordinated sites become essentially identical, bringing the spheres in inequivalent sites very close to mechanical equilibrium. Such a scheme is

**Table 1** Nine trial lattices with their corresponding space groups, number of sites per unit cell, coordination number, and an image of the deformed sphere with well-developed facets illustrating the shape of the Wigner–Seitz cell. Here, the coordination number  $z$  is the number of contacts with the nearest and next-nearest neighbors. In lattices where it varies with density we list a sequence of  $z$  values corresponding to the different regimes from small to large density. In the SH, ST, and BCT lattices, this sequence depends on the ratio of lattice parameters  $c/a$ . The shapes in the rightmost column are computed within the SVK model with a Poisson ratio of  $\nu = 0.1$  and a relative indentation of the nearest-neighbor contact zones of  $2h/\sigma = 0.5$ ; in SH, ST, and BCT lattices  $c/a = 1, 0.7$ , and  $0.85$ , respectively

Lattice	Space group	Sites per unit cell	Coordination number $z$	Wigner–Seitz cell
Simple cubic (SC)	$Pm\bar{3}m$	1	6	
Body-centered cubic (BCC)	$Im\bar{3}m$	2	8, 14	
Face-centered cubic (FCC)	$Fm\bar{3}m$	4	12	
Hexagonal close-packed (HCP)	$P6_3/mmc$	6	12	
Diamond cubic (DC)	$Fd\bar{3}m$	8	4, 16	
A15	$Pm\bar{3}n$	8	2, 6, 14 in columnar sites 0, 12, 12 in interstitial sites	
Simple hexagonal (SH) <sub>c/a</sub>	$P6/mmm$	3	2, 8 for $c/a < 1$ 8 for $c/a = 1$ 6, 8 for $c/a > 1$	
Simple tetragonal (ST) <sub>c/a</sub>	$PA/mmm$	1	2, 6 for $c/a < 1$ 6 for $c/a = 1$ 4, 6 for $c/a > 1$	
Body-centered tetragonal (BCT) <sub>c/a</sub>	$I4/mmm$	2	2, 8 for $c/a < 1/2$ 2, 10, 14 for $1/2 \leq c/a < \sqrt{2/3}$ 8, 10, 14 for $\sqrt{2/3} \leq c/a < 1$ 8, 14 for $c/a = 1$ 8, 12, 14 for $1 < c/a < \sqrt{2}$ 12 for $c/a < \sqrt{2}$	

computationally much more convenient than the full model. In the A15 lattice, the average energy per sphere is a 1:3 weighted average of the two sites so as to reflect their relative frequency.

The cell model is implemented in the FreeFEM++ finite-element-method environment.<sup>19</sup> The domain representing a sphere is tessellated by tetrahedra and the meshes are generated by the Gmsh grid generator,<sup>20</sup> with the number of nodes ranging between  $4.5 \times 10^4$  and  $5 \times 10^4$ . This resolution is sufficient for a relative numerical accuracy of the displacement field between  $10^{-5}$  and  $10^{-4}$ . The constraints are represented by steep auxiliary potentials which penalize any part of the sphere that extends beyond the Wigner–Seitz cell. In each run, we compress the sphere from small to large indentations in steps of  $\Delta(2h/\sigma) = 0.01$ . Since the SVK and NH strain energy densities are not harmonic, the problem of finding the equilibrium, minimal-energy

state is non-linear. The equilibrium state is found iteratively using the weighted Newton–Raphson method and we employ the UMF-PACK solver<sup>21</sup> to compute the displacement field in each iteration.

### 3 Beyond Hertz theory

The geometrical arguments restricting the Hertzian range (Section 1) are readily visualizable but they overestimate the Hertzian range; a more detailed insight is provided by physical criteria. Here we examine two such criteria, one based on the total energy of a sphere in a given lattice (Sections 3.1 and 3.2) and the other based on the distribution of the strain energy density across a sphere (Section 3.3). The purpose of examining these criteria is twofold: first, we wish to understand the dependence of the Hertzian range on  $\nu$  and the type of the

strain energy density, and second, by reproducing the Hertzian behavior at small indentations we verify our numerical scheme.

### 3.1 Diametral compression

In Fig. 2, we plot the reduced SVK and NH elastic energy of a diametrically compressed sphere at  $\nu = 0, 0.24$ , and  $0.48$  so as to cover all non-auxetic materials up to nearly incompressible solids. The reduced energy is rescaled by  $1 - \nu^2$ , which is proportional to the Hertzian repulsion [eqn (1)] and causes the curves to collapse at small indentations.

Fig. 2a shows that in the SVK model, the Hertzian range varies considerably with  $\nu$ . For small  $\nu$ , eqn (1) seems to describe the elastic energy rather well up to fairly large indentations, with the upper limit depending on the tolerance. A relative difference in the computed and Hertzian energies of 5% was chosen as a cutoff, which is consistent with the strain energy distribution criterion introduced in Section 3.3. With this threshold, the Hertzian ranges at  $\nu = 0, 0.24$ , and  $0.48$  terminate at  $2h/\sigma \approx 0.4, 0.2$ , and  $0.14$ , respectively. The NH model (Fig. 2b) has a narrower Hertzian range which ends at reduced indentations of  $2h/\sigma \approx 0.14, 0.12$ , and  $0.05$  at  $\nu = 0, 0.24$ , and  $0.48$ , respectively. The difference between the two models can be associated with the role of terms in eqn (2) and (3) that contain  $\ln J$ , which diverges as  $2h/\sigma \rightarrow 1$ .

### 3.2 Regular lattices

Fig. 2 shows that in a given confining geometry, the Hertzian range depends on the Poisson ratio, and geometrical arguments in Section 1 suggest that it also depends on the coordination number  $z$ . We expect that the width of the Hertzian range decreases with  $z$  because a large  $z$  implies that the (average) distance between the neighboring contact zones is small. As a result, the displacement fields of the contact zones interfere with each other at smaller indentations. This effect is illustrated in Fig. 3 where we plot the elastic energy per contact zone as a function of indentation for a diametrically compressed sphere ( $z = 2$ ) and DC ( $z = 4\frac{1}{2}$ ), SC ( $z = 6$ ), and FCC ( $z = 12$ ) lattices. We refer to these lattices as regular because the angles between the adjacent sphere–sphere bonds are all the same.

We confine ourselves to the SVK model where the variation of the elastic energy with  $\nu$  is more pronounced than that in the NH model (Fig. 2). Fig. 3 shows that at a small Poisson ratio ( $\nu = 0.1$ ; panel a), the Hertzian range is broader than that at a large Poisson ratio ( $\nu = 0.4$ ; panel b). The results obtained at  $\nu = 0.4$  also demonstrate that the Hertzian range indeed decreases with the coordination number. At  $\nu = 0.1$ , the dependence of the energy per contact zone on  $z$  is much weaker than that at  $\nu = 0.4$ . We observe an anomaly in that the SC energy exceeds the FCC energy although it has a smaller  $z$ , but the difference is small. A more striking feature of the  $\nu = 0.1$  plot is that the energies per contact zone in the DC, SC, and

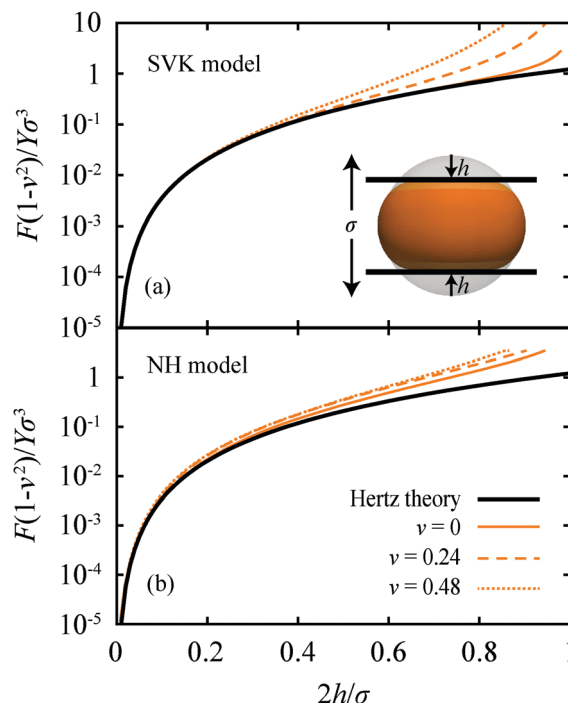


Fig. 2 Elastic energy of a diametrically compressed sphere vs. reduced indentation for the SVK and NH models (a and b, respectively) at Poisson ratios of 0, 0.24, and 0.48. The energy is scaled by  $Y\sigma^3/(1 - \nu^2)$  so as to eliminate the Hertzian dependence on  $\nu$  [eqn (1)]. The inset shows a diametrically compressed SVK sphere at  $\nu = 0.24$  and  $2h/\sigma = 0.4$ .

FCC lattices agree with each other rather well even beyond the Hertzian range.

Fig. 3 can be used to trace the limits of the Hertz theory. At 5% tolerance used in Section 3.1, the Hertzian range extends to  $2h/\sigma$  between 0.08 ( $z = 6$  and  $z = 12$ ) and 0.35 ( $z = 2$ ) at  $\nu = 0.1$  and to  $2h/\sigma$  between 0.04 (for  $z = 6$  and  $z = 12$ ) and 0.13 ( $z = 2$ ) at  $\nu = 0.4$ . As expected, the  $z = 12$  ranges are smaller than that based on geometrical arguments from Section 1, with the difference increasing with the Poisson ratio. For large- $z$  lattices, the  $z = 12$  value may be viewed as a universal rule-of-thumb estimate of the Hertzian range.

### 3.3 Strain energy density criterion: Hertzian vs. uniform-stress regime

The strain energy distribution within a deformed sphere exposes the degree of pairwise additivity more clearly than the total energy per contact analyzed in Fig. 2 and 3. Here, we discuss primarily an SVK sphere in the FCC lattice; the qualitative conclusions reached apply to all lattices in both the SVK and NH models. The cross-sections in Fig. 4a illustrate two deformation regimes. At small indentations the energy density is localized at the contact zones, with the penetration depth being small compared to the diameter. Faint instances of this pattern are visible in all three  $2h/\sigma = 0.04$  cross-sections and the more pronounced ones can be seen in the  $2h/\sigma = 0.08$  cross-section at  $\nu = 0$  and  $0.24$ . On the other hand, the  $\nu = 0.48$ ,  $2h/\sigma = 0.08$  energy density forms a ring connecting neighboring contact

‡ Using geometrical reasoning from Section 1, we estimate that the DC lattice is 4-coordinated at  $2h/\sigma$  up to  $\approx 0.36$  and 16-coordinated beyond this point. Physical arguments push the onset of the 16-coordinated regime to a lower  $2h/\sigma$ , but it is still beyond the upper limit of the range covered in Fig. 3.

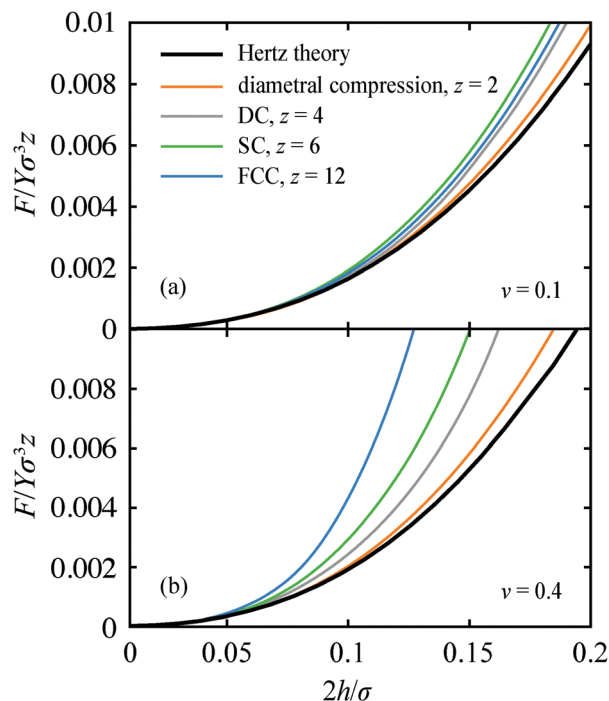


Fig. 3 Elastic energy per neighbor obtained from the SVK model for diametral compression ( $z = 2$ ) and DC, SC, and FCC lattices ( $z = 4, 6$ , and  $12$ , respectively) as a function of relative indentation at two different Poisson ratios of  $\nu = 0.1$  (a) and  $\nu = 0.4$  (b). The black line is the Hertz law  $\propto h^{5/2}$ .

zones, which shows that the total displacement field is not a simple superposition of individual indentations. This effect is more prominent in the  $\nu = 0.48$ ,  $2h/\sigma = 0.12$  cross-section where the energy density no longer peaks immediately below the contact zones but in subsurface regions bridging the zones.

As indentation is increased, the displacement field gradually penetrates deeper into the sphere, and the distribution of the strain energy density is increasingly more uniform. This behavior is exemplified by the nearly incompressible  $\nu = 0.48$  sphere at  $2h/\sigma = 0.2$ . As proposed earlier,<sup>22</sup> a deformed sphere in the uniform-stress regime may be viewed as a hard body in that stresses are transmitted without any attenuation. In other words, in this regime the stress penetration depth is much larger than the reference sphere diameter.

The onset of the uniform-stress regime depends on the Poisson ratio. At an indentation equal to  $2h/\sigma = 0.16$  (Fig. 4a) the energy density pattern at  $\nu = 0.24$  belongs to the uniform-stress regime, unlike the one at  $\nu = 0$ . To introduce a criterion defining this regime, we compare the energy density in the center of the sphere with the maximal energy density. Once their ratio exceeds 50%, we deem the sphere to be in the uniform-stress regime.<sup>§</sup> In a similar fashion, we consider the sphere to be in the Hertzian regime if the energy density at the midpoint of

the line connecting the centers of the neighboring contact zones is less than 20% of the maximal energy density.

The boundaries of the Hertzian and uniform-stress regimes obtained using these criteria are plotted in Fig. 4c which shows that in the SVK model the FCC Hertzian range depends very much on the Poisson ratio, decreasing from  $2h/\sigma = 0.08$  at small  $\nu$  to  $2h/\sigma = 0.04$  at  $\nu \rightarrow 0.5$ . Still the knee-shaped boundary of the Hertzian range is unexpected, and we cannot offer a simple explanation. On the other hand, the onset of the uniform-stress regime varies more smoothly with  $\nu$  except close to 0.5 where the sphere becomes incompressible. At  $\nu = 0.5$ , we can again resort to geometrical arguments – here the uniform-stress regime starts close to the point where the volume of the Wigner-Seitz cell equals the reference volume of the sphere, which is at  $\rho\sigma^3 = 6/\pi \approx 1.909$ , and agrees very well with our numerical results.

In other large- $z$  lattices, the boundaries of the two regimes are similar as in the FCC lattice. Naturally, the symmetry of each lattice does matter but the features defining the Hertzian and uniform-stress regimes are present in all lattices. This is illustrated by the cutaway views of the deformed SVK spheres in Fig. 4b. In the BCC lattice, the Hertzian range is slightly broader than that in the FCC lattice. As the 8 nearest-neighbor contact zones in the BCC lattice are farther apart from each other than the 12 contact zones in the FCC lattice, the BCC Hertzian range extends to larger indentations than that in the FCC lattice. In a similar manner, in the SH lattice the Hertzian range varies with the ratio of lattice parameters  $c/a$ . At  $c/a > 1$  where the 6 in-plane neighbors are closer to the reference sphere than those in adjacent planes, the cross-talk between the neighboring contact zones happens at a smaller indentation than that in the FCC lattice due to a smaller distance between the 6 in-plane contact zones compared to that between the FCC contact zones.

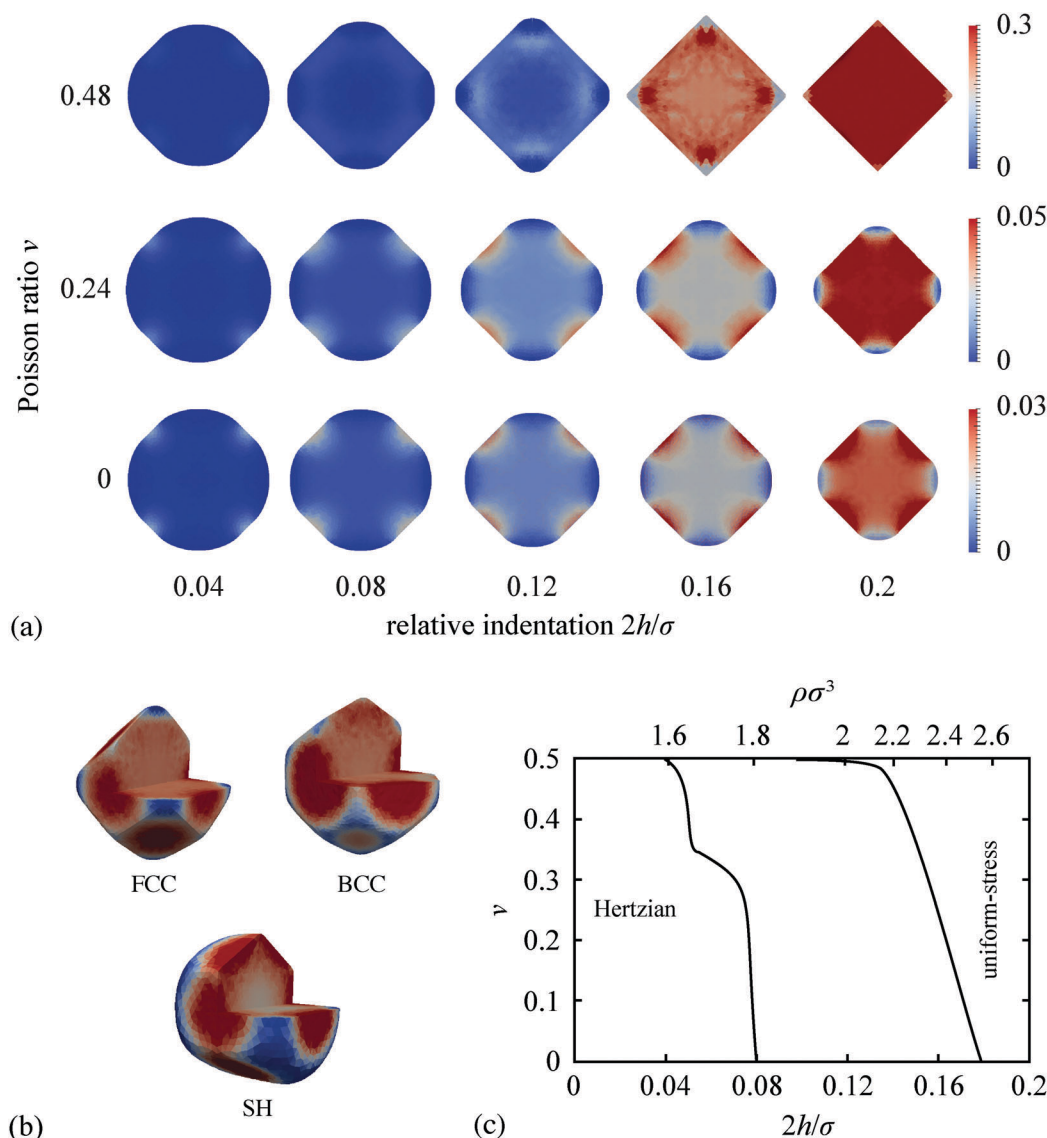
Although obtained within the SVK model, the above estimates of the physical Hertzian range are generic because they pertain to indentations where all models reduce to the small-deformation Hookean elasticity. Thus, we can conclude that the FCC Hertzian range ends at a reduced density  $\rho\sigma^3$  between 1.6 and 1.8 depending on the Poisson ratio. These reduced densities are below the FCC–BCC coexistence range obtained using the Hertz theory,<sup>12,13</sup> implying that the only meaningful result based on this theory is the fluid–FCC transition.

## 4 Phase diagram

Our main results are the SVK and NH phase diagrams in Fig. 5a and b, respectively. To construct them, we considered nine trial lattices in Table 1, varying the ratio of lattice parameters  $c/a$  in the SH, ST, and BCT lattices from 0.3 to 1, from 0.3 to 1.4, and from 0.3 to  $\sqrt{2}$ , respectively. In the two tetragonal lattices, the ranges of  $c/a$  were centered around 1 so as to see whether distortions of the corresponding cubic lattices can lower the energy – and to find that they do but not in the regime where the distorted lattices are stable. In the SH lattice, we focused on  $c/a < 1$  because in studies based on Hertzian interaction<sup>12,13</sup> this lattice was found to be stable at  $c/a \approx 0.84$ .

<sup>§</sup> The notion of the uniform-stress regime based on stress distribution is not too different from that of the complete faceting regime based on the packing fraction. Still, these two concepts are not completely identical as demonstrated in Fig. 5c.



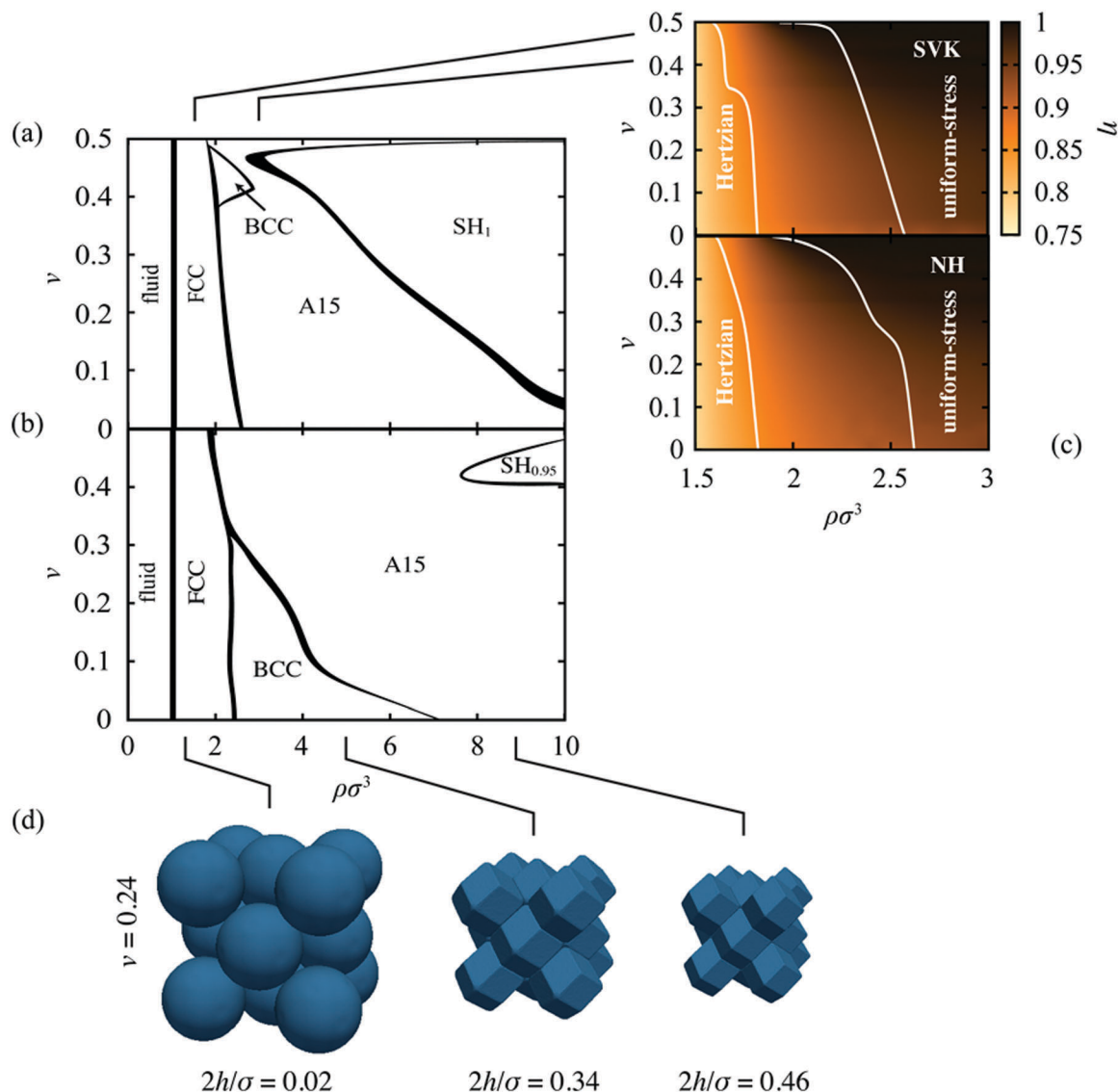


**Fig. 4** (a) Strain energy distribution in the SVK sphere in the FCC lattice in the plane containing two 4-fold axes at Poisson ratios  $\nu = 0, 0.24$ , and  $0.48$  and five relative indentations  $2h/\sigma$ . (b) At each Poisson ratio, strain energy density measured in units of  $Y$  is color-coded such that red corresponds to the largest value in the  $2h/\sigma = 0.2$  cross-section and blue corresponds to 0. Cutaway views of the SVK sphere in the FCC, BCC, and SH lattices at  $\nu = 0.3$  and  $2h/\sigma = 0.2$ . (c) Boundaries of the FCC Hertzian and uniform-stress ranges in the  $(2h/\sigma, \nu)$  plane. A secondary horizontal axis is also included to show the reduced density; this axis is non-linear.

The phase diagrams in Fig. 5a and b are rather simple in the sense that they feature only four lattices; actually five, because the elastic energies of FCC and HCP lattices are identical within numerical error in both models at all values of  $\rho\sigma^3$  and  $\nu$ . As anticipated, both SVK and NH models predict a stable FCC lattice immediately beyond the fluid–solid transition, and in both models the width of the FCC range becomes narrower as  $\nu$  is increased. The other dominant phase stable in both models and at all  $\nu$  is the A15 lattice. The BCC lattice is less generic as it intervenes between FCC and A15 only over a range of  $\nu$ : in the SVK model, the BCC pocket extends from  $\nu \approx 0.39$  to  $\nu \approx 0.49$ , whereas in the NH model it extends up to  $\nu \approx 0.32$ . The last structure present in the phase diagram is the SH lattice. Within the SVK model it is stable at virtually any  $\nu$  provided that

the density is large enough, whereas in the NH model it is restricted to  $\nu > 0.42$ . By scanning the ratio of lattice parameters  $c/a$  in steps of 0.05, we found that the SH lattice is stable at  $c/a = 1$  in the SVK model and at  $c/a = 0.95$ ; more precisely, for a narrow range of  $c/a$  that contains these values and is no wider than twice the step.

A comparison of Fig. 5a and b with the phase diagram of Hertzian spheres<sup>12,13</sup> is relevant only at small  $\rho\sigma^3$ . The reason for this is that in both SVK and NH models, the Hertzian regime ends within the region of stability of the FCC lattice and the FCC–BCC and FCC–A15 transitions are not too far from the onset of the uniform-stress regime (Fig. 5c), so they cannot be rationalized within the Hertz theory. Still these two transitions do not depend strongly on  $\nu$ , which must be due to the proximity



**Fig. 5** Phase diagram of elastic spheres in the  $(\rho\sigma^3, \nu)$ -plane within the SVK and NH models (panels a and b, respectively); the subscript in the SH lattice denotes the ratio of lattice parameters  $c/a$ . Panel c shows the boundaries of the Hertzian range and the uniform-stress regime as well as a color-coded representation of the packing fraction defined as the portion of unit-cell volume occupied by the spheres. For clarity, we only plot the FCC results; in other stable lattices the two boundaries and packing fractions are similar. The snapshots of the FCC lattice of  $\nu = 0.24$  SVK spheres at  $\rho\sigma^3 \approx 1.46, 4.92$ , and  $8.98$  illustrate the degree of compression covered by the density range studied here (d).

of the Hertzian range. Together with the presence of the FCC lattice right after the fluid phase, this seems to be the only fingerprint of the Hertzian behavior.

#### 4.1 Transitions in the uniform-stress regime

To visualize compressions covered by Fig. 5a and b, it is instructive to convert the reduced densities to sphere diameters. In spheres arranged in the FCC lattice such that they just touch, the packing fraction defined as the ratio of lattice volume filled by the spheres is  $\eta = \pi\rho\sigma^3/6 \approx 0.74$ ; here  $\rho\sigma^3 \approx 1.41$ . Now imagine increasing the density by decreasing the lattice constant and the diameter of the spheres without changing their shape: then  $\rho\sigma^3 = 10$  corresponds to a compression to about 52% of the reference diameter. In reality, such a large compression brings the

spheres deep into the complete faceting regime where their shape almost perfectly conforms to the Wigner-Seitz cell and  $\eta$  is essentially unity. This is illustrated by the snapshots in Fig. 5d as well as by Fig. 5c which shows the packing fraction together with the boundaries of the Hertzian and uniform-stress regimes. (For clarity we only plot the FCC data; those for the other lattices are just a little different.) Fig. 5c emphasizes that the SH and A15 regions and much of the BCC region are in the uniform-stress regime where  $\eta$  is very close to 1 and does not depend on compression. The surprising fact about the phase diagram is then the presence of the BCC–A15 and A15–SH transitions in this regime, which is at odds with the hard-particle view of associating the stability of a lattice with its packing efficiency.

In the uniform-stress regime, the strain energy density is dominated by terms containing the Jacobian  $J$ . At large  $\rho\sigma^3$ , say for  $\rho\sigma^3 > 3$ , these terms are virtually identical in all lattices because their packing fractions are the same. Thus, the average  $J$  must be the same in all lattices too, and in the uniform-stress regime the average  $J$  is representative of the actual  $J$ . As a result,  $J$  can only depend on the reduced density but not on the lattice, and hence the  $J$ -containing terms are the same in all lattices. Yet our results suggest that the subtle differences between the terms that do not contain  $J$  may vary with  $\rho\sigma^3$  to a large enough extent so as to drive the BCC–A15 and A15–SH transitions.

The uniform-stress regime is dominated by many-body effects and currently there exists no simple unified interpretation of all phase sequences in Fig. 5a and b. One possibility is to develop a heuristic model based on the separation of the elastic energy into bulk and surface terms.<sup>10</sup> Indeed, Fig. 4a and b suggest that the localized strain energy at the contact zones can be viewed as excess surface energy, and they also show that in the complete faceting regime the edges of the spheres should carry a negative line tension. Whether a generalized scheme from ref. 10 that would include a line-tension term or even a vertex term could work remains to be seen.

## 4.2 Robustness

Like in many solid–solid transitions, the energy differences between the lattices of elastic spheres are small which means that even a moderate numerical inaccuracy may alter the phase diagram considerably by shifting the coexistence densities obtained using the Maxwell double-tangent construction. In particular, most of the phase-coexistence densities in Fig. 5a and b are not as smooth as one would expect, and most likely the wiggles are a numerical artifact rather than a physical effect.

To estimate the inaccuracy, we recompute the diagram based on extrapolated energies  $E_\infty$  corresponding to an infinitely fine

grid and those obtained by fitting a sequence of energies with  $N$  from  $\approx 2 \times 10^3$  to  $\approx 8 \times 10^4$  by using the formula  $aN^b + E_\infty$  with  $b < 0$ . This is plotted in Fig. 6 which zooms in on the BCC region in the NH model; also included are the data points used to compute the phase diagram, demonstrating that the wiggles are not due to a sparse scan of the  $\nu$  axis. Although the extrapolated phase boundaries are shifted by up to about 10% the topology of the phase diagram remains unaltered. The large features of the BCC region are robust, and this also holds for the rest of the SVK and NH phase diagrams. The inset to Fig. 6 shows the differences between the elastic energies of the BCC and A15 lattices compared to that of FCC lattice at  $\nu = 0.24$ . These differences are at least one order of magnitude larger than the precision of our numerical results.

## 5 Conclusions

The main motivation of this work is to investigate whether elasticity can be used as a phenomenological model for determining the phase behavior of soft nanocolloids. By including many-body interactions we find that two different stress–strain models predict the presence of the non-close-packed BCC, A15, and SH lattices, which have also been observed in experiments.<sup>1–4</sup>

The results presented here are a detailed description of the phase behavior of elastic spheres that goes beyond the limits of Hertzian elasticity,<sup>12,13</sup> which is found to be applicable at densities barely beyond the fluid–solid transition. The presence of the same set of four lattices – FCC, BCC, A15, and SH – in two distinct finite-deformation strain energy densities suggests that their appearance is fairly generic. It is also worth noting that solid–solid transitions are predicted to occur deep within the complete faceting regime despite the geometrical saturation.

There are several promising extensions of this work that should be pursued in the future. By extending the set of trial lattices with the  $\sigma$  phase, it may be possible to explain why the  $\sigma$  lattice is sandwiched between the BCC and A15 lattices<sup>1</sup> in some cases, and in others it appears immediately after the fluid phase.<sup>4</sup> One could also consider finite-deformation models tailored for different materials<sup>23</sup> or include surface tension<sup>24</sup> and surface elasticity.<sup>25</sup> It would be even more intriguing to study spheres with non-uniform elastic properties, resembling core–shell nanocolloids.<sup>26,27</sup> Finally, including finite-temperature effects into the model would allow one to explore the competition between elastic energy and entropy.

## Acknowledgements

We thank J. Hasnain, S. Jungblut, C. Leitold, A. Lošdorfer Božič, N. Osterman, V. Susič, and A. Šiber for helpful discussions. We are very grateful to the FreeFEM++ and Gmsh communities for advice as well as for the development and maintenance of the software. This work was supported by the Slovenian Research Agency through Grant No. P1-0055, the Marie-Curie Initial Training Network COMPLOIDS (FP7-PEOPLE-ITN-2008 Grant

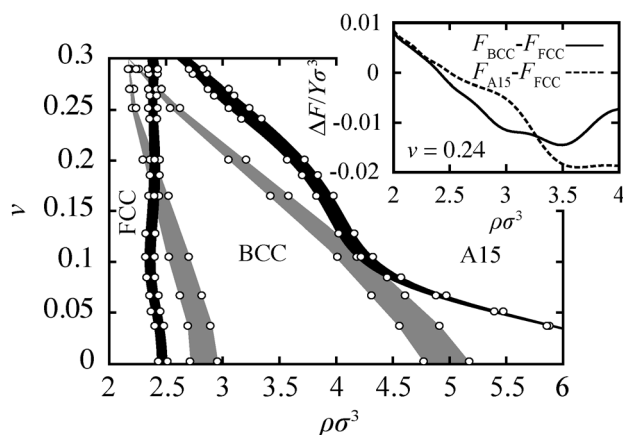


Fig. 6 Comparison of regions in the NH phase diagram centered around the BCC lattice computed using the  $N \approx 5 \times 10^4$  node energies (black) and the extrapolated  $N \rightarrow \infty$  energies (gray). Circles show the coexistence density data points used to plot the diagram. Inset: Energies of BCC and A15 lattices relative to the energy of the FCC lattice at  $\nu = 0.24$  and  $N \approx 5 \times 10^4$ .



No. 234810), and the Marie-Sklodowska-Curie European Training Network COLLDENSE (H2020-MSCA-ITN-2014 Grant No. 642774).

## References

- 1 X. Zeng, G. Ungar, Y. Liu, V. Percec, A. E. Dulcey and J. K. Hobbs, *Nature*, 2004, **428**, 157.
- 2 S. Lee, M. J. Bluemle and F. S. Bates, *Science*, 2010, **5**, 330.
- 3 C. Tschierske, *Angew. Chem., Int. Ed.*, 2013, **52**, 8828.
- 4 S. Chanpuriya, K. Kim, J. Zhang, S. Lee, A. Arora, K. D. Dorfman, K. T. Delaney, G. H. Fredrickson and F. S. Bates, *ACS Nano*, 2016, **10**, 4961.
- 5 S. Fischer, A. Exner, K. Zielske, J. Perlich, S. Deloudi, W. Steurer, P. Lindner and S. Förster, *Proc. Natl. Acad. Sci. U. S. A.*, 2011, **108**, 1810.
- 6 T. M. Gillard, S. Lee and F. S. Bates, *Proc. Natl. Acad. Sci. U. S. A.*, 2016, **113**, 5167.
- 7 Y. Y. Li, S. T. Lin and W. A. Goddard, *J. Am. Chem. Soc.*, 2004, **126**, 1872.
- 8 C. R. Iacovella, A. S. Keys and S. C. Glotzer, *Proc. Natl. Acad. Sci. U. S. A.*, 2011, **108**, 20935.
- 9 M. Watzlawek, C. N. Likos and H. Löwen, *Phys. Rev. Lett.*, 1999, **82**, 5289.
- 10 P. Ziherl and R. D. Kamien, *Phys. Rev. Lett.*, 2000, **85**, 3528.
- 11 L. D. Landau and E. M. Lifshitz, *Theory of Elasticity*, Butterworth-Heinemann, Oxford, 3rd edn, 1986.
- 12 J. C. Pàmies, A. Cacciuto and D. Frenkel, *J. Chem. Phys.*, 2009, **131**, 044514.
- 13 S. Prestipino, F. Saija and G. Malescio, *Soft Matter*, 2009, **5**, 2795.
- 14 G. A. Holzapfel, *Nonlinear Solid Mechanics, A Continuum Approach for Engineering*, John Wiley & Sons, Chichester, 2000.
- 15 J. Bonet and R. D. Wood, *Nonlinear Continuum Mechanics for Finite Element Analysis*, Cambridge University Press, Cambridge, 2nd edn, 2008.
- 16 L. R. G. Treloar, *Trans. Faraday Soc.*, 1943, **39**, 241.
- 17 L. R. G. Treloar, *Trans. Faraday Soc.*, 1946, **42**, 83.
- 18 R. S. Rivlin, *Philos. Trans. R. Soc. London, Ser. A*, 1948, **240**, 459.
- 19 F. Hecht, *J. Numer. Math.*, 2012, **20**, 251.
- 20 C. Geuzaine and J.-F. Remacle, *Int. J. Numer. Meth. Eng.*, 2009, **79**, 109.
- 21 T. Davis, *ACM Trans. Math. Softw.*, 2004, **30**, 196.
- 22 A. Šiber and P. Ziherl, *Phys. Rev. Lett.*, 2013, **110**, 214301.
- 23 M. C. Boyce and E. M. Arruda, *Rubber Chem. Technol.*, 2000, **73**, 504.
- 24 J. Riest, L. Athanasopoulou, S. A. Egorov, C. N. Likos and P. Ziherl, *Sci. Rep.*, 2015, **5**, 15854.
- 25 P. Sharma, S. Ganti and N. Bhate, *Appl. Phys. Lett.*, 2003, **82**, 535.
- 26 R. L. Whetten, M. N. Shafigullin, J. T. Khoury, T. G. Schaaff, I. Vezmar, M. M. Alvarez and A. Wilkinson, *Acc. Chem. Res.*, 1996, **32**, 397.
- 27 M. A. Boles, M. Engel and D. V. Talapin, *Chem. Rev.*, 2016, **116**, 11220.